



Article

SkySat Data Quality Assessment within the EDAP Framework

Sebastien Saunier¹, Gizem Karakas², Ilyas Yalcin^{2,3} , Fay Done⁴, Rubinder Mannan⁴, Clement Albinet⁵, Philippe Goryl⁵ and Sultan Kocaman^{6,7,*}

¹ Telespazio France, 26 Avenue Jean François Champollion, 31100 Toulouse, France; sebastien.saunier@telespazio.com

² Graduate School of Science and Engineering, Hacettepe University, 06800 Beytepe, Ankara, Turkey; gizem.karakas@hacettepe.edu.tr (G.K.); ilyas.yalcin@hacettepe.edu.tr (I.Y.)

³ Baskent OSB Technical Sciences Vocational School, Hacettepe University, 06909 Sincan, Ankara, Turkey

⁴ Telespazio UK Ltd., 350 Capability Green, Luton, Bedfordshire LU1 3LU, UK; fay.done@telespazio.com (F.D.); rubinder.mannan@telespazio.com (R.M.)

⁵ European Space Agency, ESRIN, Via Galileo Galilei, 1, 00044 Frascati, RM, Italy; clement.albinet@esa.int (C.A.); philippe.goryl@esa.int (P.G.)

⁶ Department of Geomatics Engineering, Hacettepe University, 06800 Beytepe, Ankara, Turkey

⁷ ETH Zurich, Institute of Geodesy and Photogrammetry, 8093 Zurich, Switzerland

* Correspondence: sultankocaman@hacettepe.edu.tr

Abstract: Cal/Val activities within the Earthnet Data Assessment Pilot (EDAP) Project of the European Space Agency (ESA) cover several Earth Observation (EO) satellite sensors, including Third-Party Missions (TPMs). As part of the validation studies of very-high-resolution (VHR) sensor data, the geometric and radiometric quality of the images and the mission compliance of the SkySat satellites owned by Planet were evaluated in this study. The SkySat constellation provides optical images with a nominal spatial resolution of 50 cm, and has the capacity for multiple visits of any place on Earth each day. The evaluations performed over several test sites for the purpose of the EDAP Maturity Matrix generation show that the high resolution requirement is fulfilled with high geometric accuracy, although various systematic and random errors could be observed. The 2D and 3D information extracted from SkySat data conform to the quality expectations for the given resolution, although improvements to the vendor-provided rational polynomial coefficients (RPCs) are essential. The results show that the SkySat constellation is compliant with the specifications and the accuracy results are within the ranges claimed by the vendor. The signal-to-noise ratio assessments revealed that the quality is high, but variations occur between the different sensors.

Keywords: Earth Observation; data quality; SkySat; geometric validation; radiometric validation; maturity matrix



Citation: Saunier, S.; Karakas, G.; Yalcin, I.; Done, F.; Mannan, R.; Albinet, C.; Goryl, P.; Kocaman, S. SkySat Data Quality Assessment within the EDAP Framework. *Remote Sens.* **2022**, *14*, 1646. <https://doi.org/10.3390/rs14071646>

Academic Editors: Mohammadmehdi Saberioon and Daniel Spengler

Received: 3 February 2022

Accepted: 27 March 2022

Published: 29 March 2022

Publisher's Note: MDPI stays neutral with regard to jurisdictional claims in published maps and institutional affiliations.



Copyright: © 2022 by the authors. Licensee MDPI, Basel, Switzerland. This article is an open access article distributed under the terms and conditions of the Creative Commons Attribution (CC BY) license (<https://creativecommons.org/licenses/by/4.0/>).

1. Introduction

The increasing number and diversity of Earth Observation (EO) satellite missions operated by various agencies and commercial bodies has led to the requirement of a platform to enable communication between providers. In order to ensure the coherence of the missions and their integration into the overall EO strategy, a coordination framework was defined by European Space Agency (ESA) for Third-Party Missions (TPM) within the Earthnet Programme, which has contributed to the Global Earth Observation System of Systems (GEOSS) for over 40 years [1]. The Earthnet Data Assessment Pilot (EDAP) project aimed to validate the data quality for various missions [2]. The calibration and validation (Cal/Val) tasks in the EDAP were defined in a sensor-specific manner [3]. One of the main outcomes of the project was the Maturity Matrix (MM) framework, which was initially developed within the EDAP and advanced jointly with National Aeronautics and Space Administration (NASA), Washington, DC, USA. The MM provides clear guidelines on the Cal/Val activities of the product and outputs reports on the quality and the

suitability of satellite missions on the basis of their mission specifications and potential applications [4].

The SkySat constellation from Planet, CA, USA, is composed of 21 satellite missions operating in orbit at the time of writing. After the launch of the SkySat A and B generations in 2013 and 2014, respectively, the first SkySat C-generation satellite was launched in 2016. SkySat was the first commercial microsatellite with sub-meter accuracy [5]. All SkySat C-generation sensors have similar electro-optics, with a focal length of 3.6 m and 5.5 megapixel Complementary Metal Oxide Semiconductor (CMOS) detectors [6] that facilitate the provision of continuous EO data with a small temporal interval and high consistency. Besides the 4 band multispectral (MS) imagery, the pushframe sensor structure enable the High-Definition (HD) full-frame rate panchromatic video acquisition with a 1 m ground sample distance (GSD) [6]. The main objectives of the mission include the acquisition of very high spatial resolution (i.e., enhanced 50 cm spatial resolution) MS images and video data with rapid revisit time (multiple revisits per day).

The SkySat Cal/Val tasks defined within the EDAP aimed at the fulfillment of the MM analysis requirements. The EDAP Best Practice Guidelines [7] and EDAP Optical Mission Quality Assessment Guidelines [8] were in principle followed for the requirement analysis and MM preparation. For this purpose, besides a review of the documentation (e.g., the review in [6] and the Planet L1 Data Quality Report Q3 [9]), extensive data (including metadata) investigations were carried out with the aim of assessing the image radiometric and geometric quality over various test sites. In addition to the Cal/Val reports provided by the vendor [9] and the collaborators (e.g., [10–12]), the results reported in the literature [13–17] were analyzed as well. On the other hand, mission specific assessments, e.g., stereoscopic capability in the case of SkySat data, were also performed using state-of-the-art processing methods.

Consequently, the main aims of this study are (a) to investigate the geometric and radiometric quality of SkySat products acquired over several EDAP test sites and at different product levels; (b) to discuss the issues related to the data and metadata with respect to the instrument specifications and the literature; and (c) to present the EDAP MM assessment results and potential improvements to the sensor data. Although several studies in the literature (i.e., [13–17]) have analyzed the radiometric and geometric quality of different SkySat products for various purposes, such as surface reconstruction from still and video images, resolution improvement methods, etc., using data acquired over one or two sites, this is the first comprehensive assessment of the SkySat constellation covering various Cal/Val aspects (i.e., radiometry, geometry, visual interpretation) at the same time using data acquired from multiple satellites and over multiple sites. In addition, the concept of MM developed as part of the EDAP is explained in detail and the SkySat MM is presented.

The image quality assessment efforts included the determination of the General Image Quality Equation (GIQE) parameters, which were developed for the quantitative measurement of the quality of raw or processed aerial imagery [18]. A scale consisting of ten levels has been developed by the National Image Interpretability Rating Scale (NIIRS) for detecting and interpreting objects contained in visible, radar, infrared, and multispectral imagery [19]. The GIQE parameters allow these scale values to be calculated quantitatively. The Signal-to-Noise Ratio (SNR), Signal-Difference-to-Noise Ratio (SDNR), Relative Edge Response (RER), Ground Sample Distance (GSD), and Modulation Transfer Function (MTF) are among the main GIQE parameters [20]. In this study, the SNR, RER and MTF values were analyzed over an artificial target. In addition, visual checks were performed over multiple test sites.

The geometric quality assessments include absolute and temporal geolocation accuracy, band-to-band registration (BBR) accuracy, and the quality of digital surface model (DSM) generation. The geometric quality aspects evaluated here were selected on the basis of their importance to users and their significance in the literature (e.g., see [21,22]). The methods were determined on the basis of the data format, data availability, and product

levels (e.g., geometrically raw or rectified, provision of sensor model parameters or rational functional model coefficients, etc.).

The absolute radiometric calibration quality was also assessed using one of the Pseudo-Invariant Calibration Sites (PICS), i.e., the Libya-4 site, that were employed by the Committee on Earth Observation Satellite (CEOS) for radiometric Cal/Val activities. The site was first utilized for calibration of the Satellite Pour l'Observation de la Terre (SPOT) [23], and has demonstrated proven potential for acquiring optical visible and near-infrared (NIR) images with various resolutions [24–27]. The average SNR and the SDNR values were also computed over this site and evaluated in comparison with the results of the vendor.

The article is organized as follows. The detailed sensor specifications, the test site and data characteristics, and the methods are given in the next section. The results are presented in Section 3. The discussion and conclusion are provided in the final section.

2. Materials and Methods

2.1. The SkySat Constellation

Among the satellite constellations of Planet, SkySat provides very-high-resolution (VHR) imagery. The satellites belonging to the SKS-C family ($60 \times 60 \times 95$ cm) acquire VHR data with the capacity for data collection over large areas, e.g., thousands of square kilometers. The satellites are stabilized in three axes and have the agility to observe different regions of interest (ROI) [6]. In addition, they are equipped with systems for orbital and attitude control [28] and Cassegrain telescopes [6]. In accordance with the principles of push broom imaging, the frame images (scenes) are acquired continuously in five bands, namely blue, green, red, NIR, and panchromatic (Table 1). The SkySat constellation has three cameras per satellite with identical focal plane arrangements and acquires images as overlapping strips. Half of the detector takes images in the panchromatic (Pan) channel, while the other half is split into the four multispectral (MS) bands. In accordance with the principles of pushframe imaging, every pixel is composed of up to 20 acquisitions, and a virtual time-delayed integration (TDI) method is implemented for image registration and fusion [15].

Table 1. The main characteristics of the SkySat constellation and the sensors [5,29].

Parameter	Value
Number of satellites	21
Orbit/Altitude	Polar sun-synchronous/400–600 km
Sensor/Size	Frame CMOS with TDI/5.5 megapixel
Number of sensor	3
Sensor type	Pushframe
Bands	Panchromatic: 0.450–0.900 μm
	Blue: 0.450–0.515 μm
	Green: 0.515–0.595 μm
	Red: 0.605–0.695 μm
	NIR: 0.740–0.900 μm
Focal length	3.6 m
Image capacity	400 km^2 /per day
Swath width	5.5–5.9–8 km at nadir
Image strip length (max.)	200 km
Data collection GSD	0.6–1 m
Radiometric resolution	11 bit [5]
Products	Basic Analytic Scene (BAS), Ortho Scene (OS), Ortho Collect (OC), Video

The GSD of the images at data collection depend on the spectral band and on the acquisition configuration. The recent SkySat products have been acquired in Push-broom High Dynamic Range (PBHDR) mode, which enabled higher GSDs. The PBHDR mode alters the acquisition configuration of the platform and the optical system, and is not a post-processing approach for resolution enhancement. The approach artificially reduces

the scan rate with camera vibration according to the platform velocity and the frame rate. The method also improves the SNR of the images. Thus, the resolution can be increased to 50 cm for ortho products (both MS and Pan).

The SkySat images are provided at different processing levels, such as basic analytic scene (BAS), various ortho scene (OS) products (e.g., panchromatic, visual, pan-sharpened, analytic), and ortho collect (OC) products [6]. The latter product type is a mosaic formed from individual OSs. The BAS products are suitable for DSM generation, and rational polynomial coefficient (RPC) files are provided together with the images. An orthorectification process is performed by Planet to obtain OS products by using ground control points (GCPs) and digital elevation models (DEMs) with 30 m or 90 m resolution, depending on the area [6].

2.2. Test Site Characterization and Data

In this study, the Level 1A (BAS), Level 1C (OS), and Level 1C_C (OC data formed with 20 OS from each of the three cameras) products of different SkySat satellites were evaluated with respect to their radiometric and geometric quality. The GSDs of the employed products varied depending on the satellite altitude. The collected GSDs ranged from 0.6 m and 0.7 m for the BAS, and the OC products had a resolution of 0.5 m. The test sites were selected on the basis of the land use/land cover (LULC) characteristics and the availability of the equipment (i.e., MTF target, GCPs, etc.). The geographical distribution of the test sites, which were located in Turkey, Libya and France, is presented in Figure 1. The main characteristics of the data analyzed here are summarized in Table 2. In the table, acronyms were used as test site identifiers. Multiple acquisitions from different SkySat (SKS) missions over each site were used for the evaluations. The levels of the products analyzed over each site are also given in the table, together with the type of assessment performed for each product. The assessment types include geometric validation (GeoVal), visual checks (Vis), MTF, SNR, RER, and radiometric validation (RadVal), as presented in Figure 1. The Libya-4 PICS test site (called Libya) used here is categorized as a “bright” site characterized by a highly reflective surface [30].

The GeoVal activities were performed over the Ankara test site. The GCP distribution, along with a schematic representation of the SkySat scene footprints on the OC products at this site, is presented in Figure 2. This site was used extensively for GeoVal, including stereoscopic capability assessment. A reference DSM obtained from unmanned aerial vehicle (UAV) images with 3 cm GSD was used for the comparison with the SkySat DSM.

On the other hand, the SkySat image quality was compared with pan-sharpened Pleiades images acquired over the Salon de Provence test site, France. The Pleiades images were acquired on 25 September 2014. Furthermore, Sentinel-2A MS image products acquired over Libya were employed as a reference for the RadVal activities. The Sentinel-2 satellite products were acquired on forty different dates in 2019 and 2020.

Table 2. The main features of the SkySat data used in the study.

Test Site ID	Location	Acquisition Date	Satellite	GSD (m)	Product Level	Assessment Type
ANK	Ankara, Turkey (Lat: 39.160°N, Lon: 33.472°E)	18 Jul 2020	SKS4	0.71	OC & BAS ¹	GeoVal & Vis
		23 Sep 2020	SKS7	0.66	OC & BAS ¹	GeoVal & Vis
		27 Sep 2020	SKS12	0.71	BAS ¹	GeoVal & Vis
SAL	Salon de Provence, France (Lat: 44.010°N, Lon: 4.197°E)	14 Mar 2021	SKS4	0.66	OS pan-sharpened	Vis
		29 Dec 2020	SKS17	0.57	BAS ¹	MTF & SNR & RER

Table 2. Cont.

Test Site ID	Location	Acquisition Date	Satellite	GSD (m)	Product Level	Assessment Type
LIB	Libya (Lat: 30.341°N Lon: 22.805°E)	5 Sep 2020	SKS10	0.70	BAS ¹	RadVal
		11 Sep 2020	SKS1	0.73	BAS ¹	RadVal
		17 Sep 2020	SKS7	0.67	BAS ¹	RadVal
		25 Sep 2020	SKS7	0.67	BAS ¹	RadVal
		26 Sep 2020	SKS10	0.72	BAS ¹	RadVal

¹ OC: Ortho Collect; OS: Ortho Scene; BAS: Basic Analytic Scene.

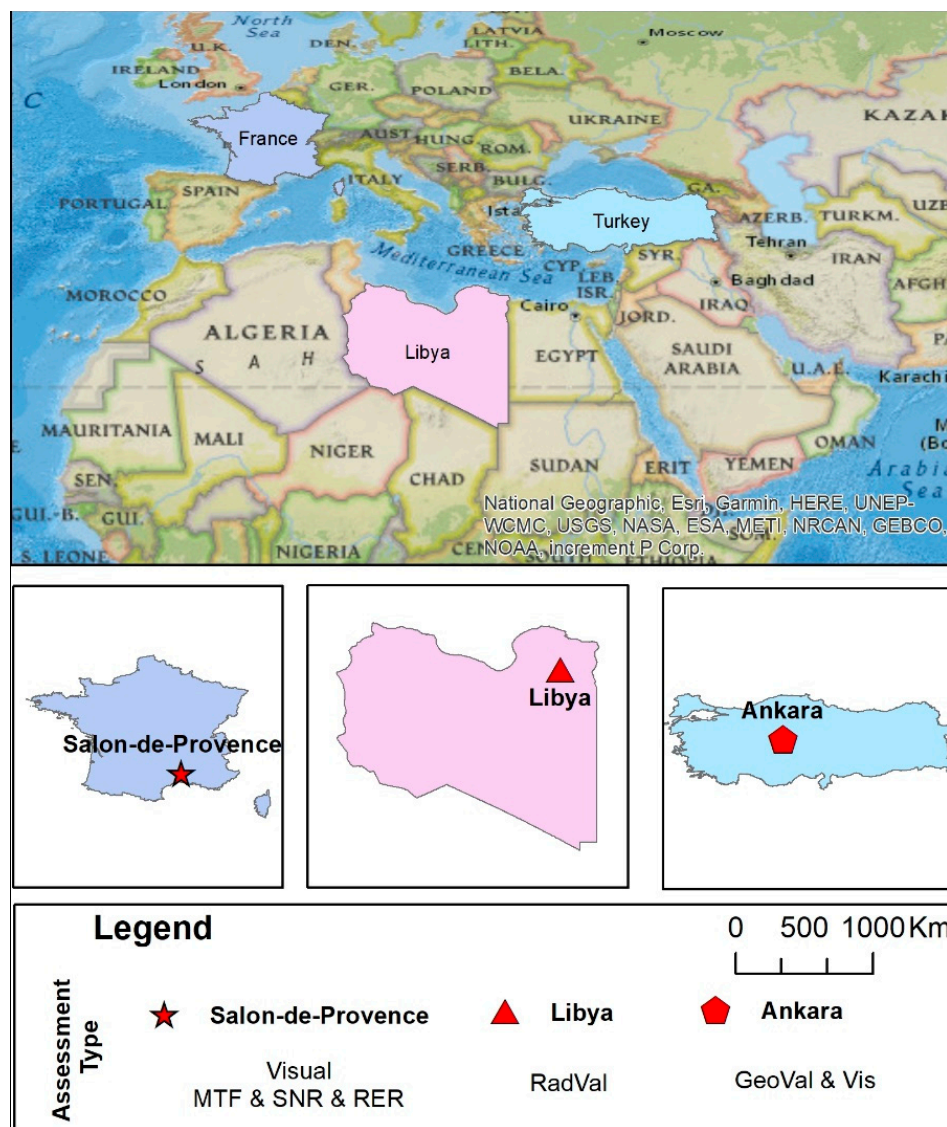


Figure 1. The locations of the EDAP test sites used in this study.

2.3. The EDAP Maturity Matrix

The overall EDAP framework covers optical, synthetic aperture radar (SAR), and atmospheric instruments [7]. While the Cal/Val MMs produced within the framework of the EDAP assignments aim at providing a high-level summary, the sub matrices generated through the validation activities present the detailed analysis results to the users for the selected missions and associated tasks, depending on the mission objectives. The Optical Mission Quality Assessment Guidelines [8] are followed for the production of high-level Cal/Val MM, and these include categories related to product and ancillary information,

product generation, uncertainty characterization, and validation. Each category is graded depending on the compliance with the FAIR (findable, accessible, interoperable, reusable) principles by means of six different grades: Not Assessed (outside the scope), Not Assessable (information not available), Basic (does not follow the FAIR principles), Intermediate (partially follows the FAIR principles), Good (largely follows the FAIR principles), and Excellent (fully FAIR compliant) [8].

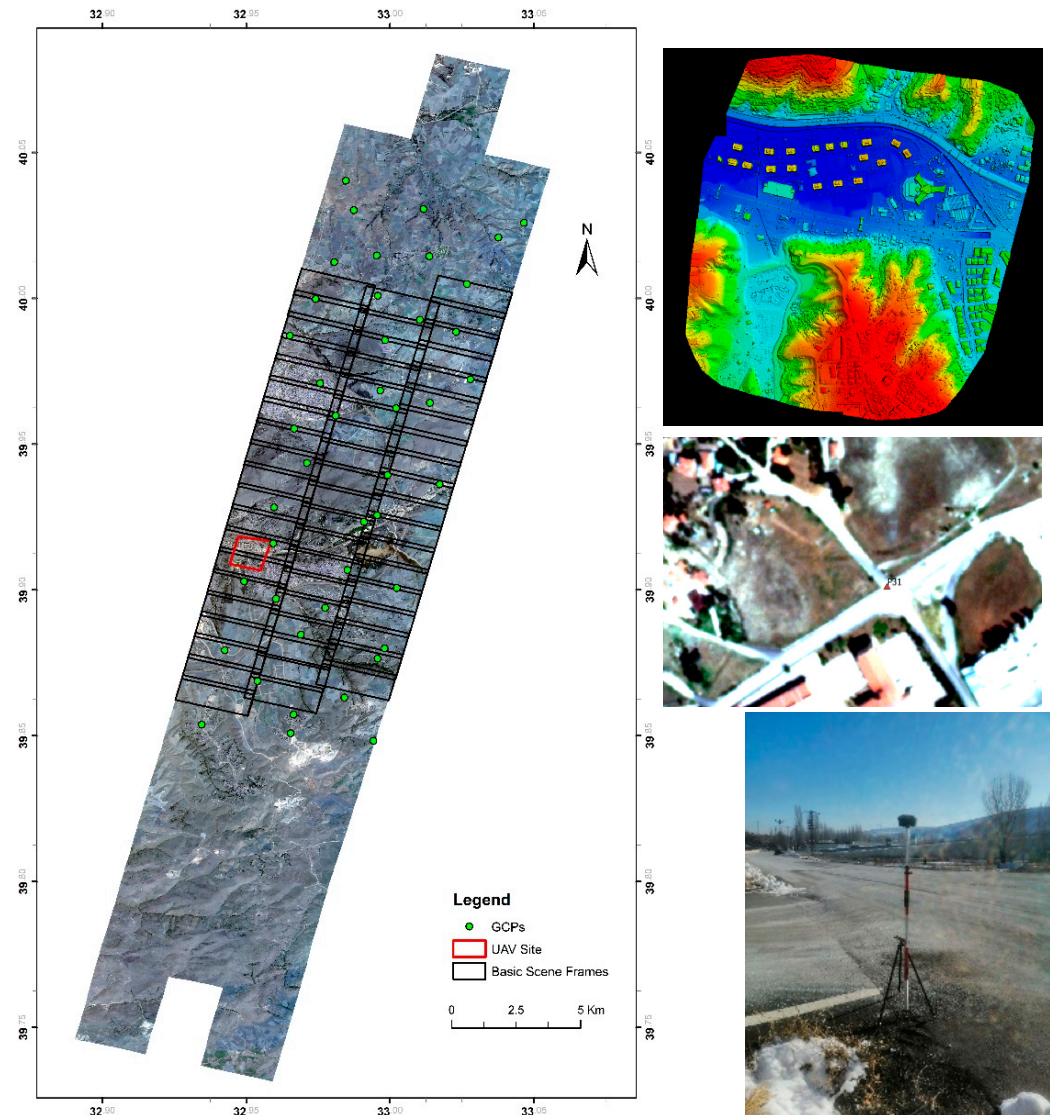


Figure 2. An overview of the SkySat Collect data acquired over the Ankara test site on 18 July 2020 with the GCP distribution (left); and the reference UAV DSM and a GCP located on the SkySat Collect image and on the ground (right).

Due to the innovative and challenging technology represented by SkySat data, the detailed quality assessments were performed on the basis of a product documentation and format evaluation, image quality, and geometric and radiometric calibration. Evaluations of the product documentation and the format were carried out by means of document and metadata reviews. Detailed assessments of image quality and geometric and radiometric calibration were carried out via visual checks, comparison with external reference data, and by using various radiometric and geometric image processing methods, as explained in the following sections.

2.4. Image Quality Assessment Approaches

The approaches for assessing image quality include visual inspection, MTF, SNR, Full Width at Half Maximum (FWHM), and RER analyses. The visual inspection addresses the unusable data mask (UDM) content and the image interpretability components. The UDM provided by the vendor often includes image backfill, cloud, and missing data information. The interpretability was analyzed in selected image sub-areas with respect to an external reference, i.e., Pleiades top of atmosphere (TOA) images. The assessments were carried out for the detection and identification of both objects and textural content. The object delineation and interpretation performances using pan-sharpened SkySat and Pleiades data were anticipated to be similar due to their identical spatial resolution (0.5 m). The selected features (points of interest) included an MTF target and different LULC types, such as transportation elements, large construction sites, forests, airports, crop fields, buildings and other urban structures, etc. Further details on the methods are provided in the following subsections.

2.4.1. SNR Computation

The SNR is an important image quality indicator [20]. Although a high SNR may not affect visual interpretation, it is an important parameter for reducing uncertainty in image measurement. The SNR is a mean value, and two types of SNR, i.e., temporal and spatial, are typically analyzed in the literature. The basic formulation of the SNR used here is given in Equation (1).

$$SNR = \frac{\mu}{\sigma} \quad (1)$$

where

- μ —mean signal; and
- σ —standard deviation of the signal.

Here, the spatial SNR over the Libya site was computed via image patches with a size of 9×9 pixels. The average (μ) and the σ of the intensity values within the patches were calculated for each spectral band (radiance). This method was first developed by Zanoni [31], and was adapted by performing patch selection in homogeneous and flat areas. As this method was applied over the Libya site, which high spatial image frequencies (e.g., desert dune summits) exist, a Sobel operator was applied to detect and eliminate the high-frequency content. Thus, patches with low-frequency content could be filtered and used. To fulfill both conditions, the proposed algorithm employed the Sobel-filtered edge image and a DEM. After eliminating unsuitable windows, the frequency distribution (histogram) of the remaining ones was used for histogram analysis. The peak value and the mean radiance value are reported for system SNR, and are presented with graphics as a function.

Although high SNR values are expected from Libya due to its bright surface, a noise model could not be obtained from a single site. On the other hand, the differential SNR (gSNR) [9], also referred to as Signal-Difference-to-Noise Ratio (SDNR) [18], was documented by the vendor. The SDNR is the ratio of the signal difference between two Lambertian surfaces and its noise (Equation (2)). The noise is often computed for the highest reflectance by using high (ρ_2) and low (ρ_1) reflectance values.

$$SDNR = \frac{S(\rho_2) - S(\rho_1)}{N(\rho_2)} \quad (2)$$

where

- $S(\rho)$ —signal;
- $N(\rho)$ —noise; and
- ρ_1, ρ_2 —reflectance values of the Lambertian targets.

The SNR value can also be defined using the approach presented in Equation (3). An approximation between gSNR and SNR is proposed by [18] and presented in Equation (4).

$$SNR = \frac{S(\rho)}{N(\rho)} \quad (3)$$

$$SDNR \approx SNR(\rho) \cdot \frac{0.08}{\sqrt{0.15 \cdot \rho}} \quad (4)$$

2.4.2. MTF Computation

Although the spatial resolution of a sensor can be associated with the GSD or Instantaneous Field of View (IFOV), its determination can be challenging for imaging sensor systems. The MTF and SNR are often assessed together as image quality metrics. As a measure of image sharpness, MTF needs to be analyzed separately for the data taken from each orbit to ensure that the quality is not degraded through vibration, medium changes (air to vacuum), or thermal alterations [32]. Although several different approaches exist, the slanted edge method [32], which analyzes the MTF, the RER and the FWHM values, was used here with a specifically designed MTF target at the Salon de Provence test site. The evaluations were carried out for the MS channels. To obtain the MTF, the Edge Spread Function (ESF) and Line Spread Function (LSF) were computed first in a direction normal to the edge. In the case of a slanted edge (with a slope in the image), the mean values of several sample patches were used, as shown in Figure 3.

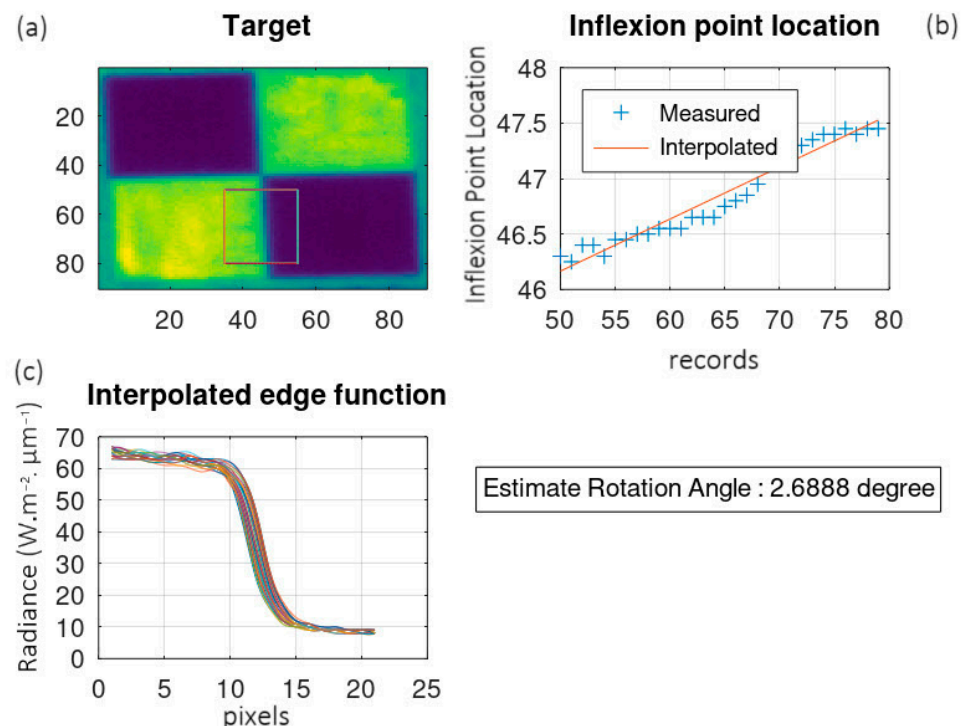


Figure 3. Slant-edge method—edge modeling output: (a) the MTF target and the selected image area (red rectangle) for the ESF analysis; (b) the line fitting output; and (c) the interpolated edges.

Assuming that the point spread function (PSF) is separable, it is possible to characterize the sensor behavior by using a 1D LSF model associated with each detector dimension (i.e., in the along-track direction and across-track direction). Considering a satellite with a sun-synchronous descending orbit, the objectives was to measure the MTF (i) in the along-track direction (AL MTF), assessed using a nearly horizontal (H) edge, and (ii) in the across-track direction (AC MTF), assessed using a nearly vertical (V) edge. Since a checkerboard target was used, the values of AL and AC MTF were computed twice depending

on the location of the region of interest in the checkboard, and in particular, contrast due to the change from high to low sensor response (i.e., the ‘l’ configuration) or from low to high sensor response (the ‘h’ configuration). The purpose was to reflect either the transition from high to low sensor response values or from low to high sensor response values. The along-track (AL)/across-track (AC) directions were also assessed separately with respect to their spatial resolution. The four directions of assessment can briefly be summarized as (i) Vl–AL (vertical) edge from high to low; (ii) Vh–AL (vertical) edge from low to high; (iii) Hl–AC (horizontal) edge from high to low; and (iv) Hh–AC (horizontal) edge from low to high sensor response.

Several parameters drive the selection of the window for performing the MTF calculations. The window parameters are presented in Figure 4 [33]. The parameter descriptions are as follows:

- ΔL —the differential radiance between the dark and bright part of the target.
- L_w —the width of the target in the direction of the MTF profile.
- α —the orientation angle α with respect to the direction of the MTF profile.
- L_H —the height of the target in the orthogonal direction of the MTF profile.

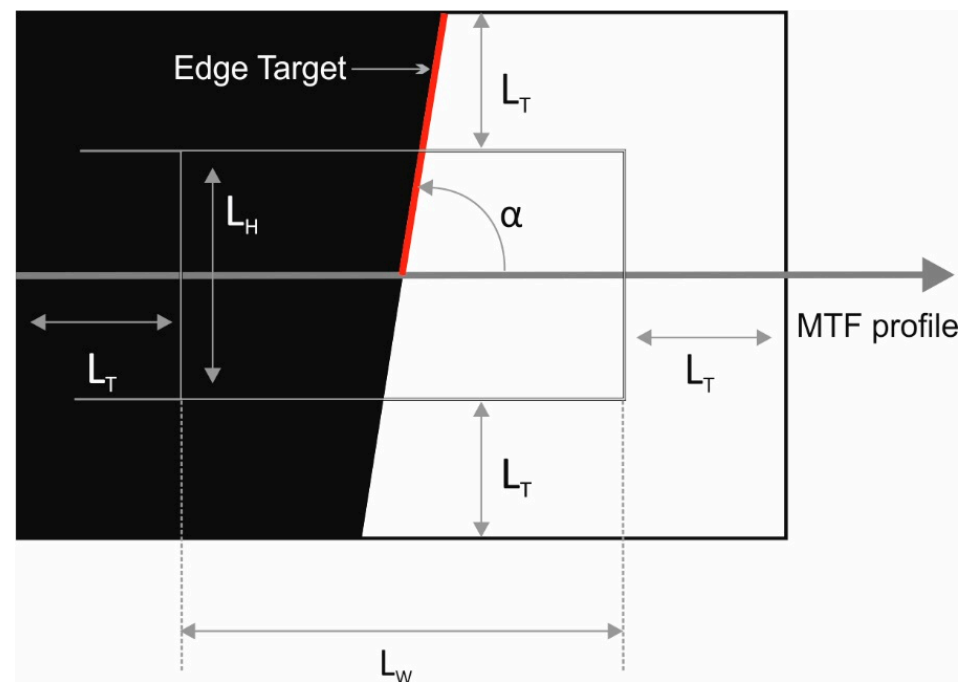


Figure 4. Schematic representation of the parameters for edge target selection (image courtesy [33]).

The ESF calculation proposed by Kohm [34] uses the measurements for both orientations (AL and AC). As an example, edge interpolation was performed for every line for the area shown with a red rectangle in Figure 3a. Afterwards, parametric functions were fitted in order to estimate the bottom of the inflection point, and least squares fitting was used to obtain the rotation (Figure 3b). The edge functions (Figure 3c) were finally analyzed, and noisy measurements were eliminated.

Because the MTF approach can be affected by noise, aliasing, and phase effects, and the edge rotation angle needs to be calculated with high accuracy, to this end, multiple image lines were analyzed. Each sample was projected on a line normal to the edge by using the angle with a bin size of 0.25 pixels (upsampled). To avoid empty bins, the selection of the right rotation angle is important. On the other hand, due to the empty bins, the distribution of the samples for ESF can be irregular. The LOcally WEighted Scatter-plot Smoother (LOESS) curve-fitting algorithm with a second-order polynomial was employed for resampling to obtain a regular distribution. It must be noted that the

proposed approach is non-parametric, which makes it possible to obtain results that are closer to system behavior by including the noise.

The LSF was computed from the ESF. To eliminate outliers, a smoothing approach via fourth-order Savitsky Golay filtering with a window size of 11 bins and a Hann window was performed. Sample ESF, LSF, ESF, and MTF graphs obtained from the analysis are presented in Figure 5. Further details on the application of the approach can be found in [32,35,36].

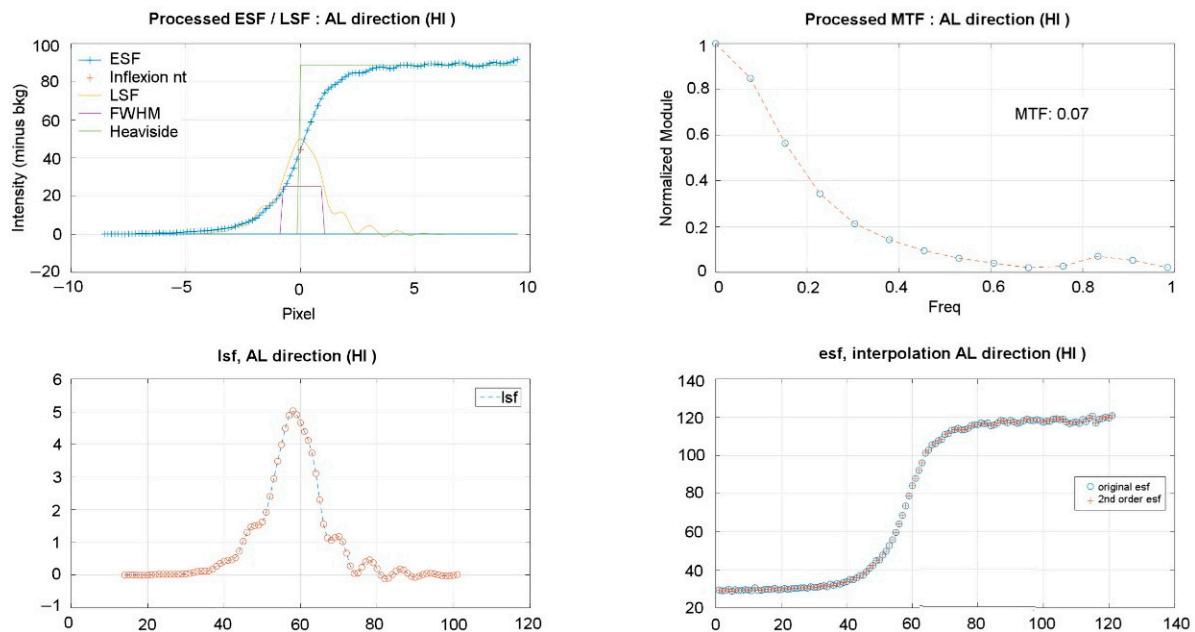


Figure 5. The output graphs of the MTF processing.

On the other hand, the SNR was also computed using the MTF target at the Salon de Provence test site. This approach uses ESF, and the mathematical expression used for this purpose is given in Equation (5).

$$SNR = \frac{|\overline{X_{high}} - \overline{X_{low}}|}{\frac{\sigma(X_{high}) + \sigma(X_{low})}{2}} \quad (5)$$

where:

- X_{high} is the statistical variable of the ESF high-intensity (radiance) values;
- X_{low} is the statistical variable of the ESF low-intensity (radiance) values; and
- $(\overline{X}, \sigma(X))$ are the corresponding statistics.

The high- and low-intensity regions are averaged from three pixels from the inflexion point of the curve, and the cardinality of high- and low-intensity samples is the same.

2.5. Radiometric Calibration Quality Assessment Approach

The radiometric calibration quality of SkySat data was assessed by comparing the reference data obtained from Sentinel-2 satellites, as they possess high accuracy, i.e., a low level of uncertainty (<3%). The TOA measurements simulated from the reference data (Figure 6) were compared for the assessment. The bottom of atmosphere (BOA) data were processed to obtain the TOA values by (i) estimating the Bidirectional Reflectance Distribution Function (BRDF) model; (ii) generating the spectrum over spectral interval; (iii) computing the TOA values by using the Second Simulation of the Satellite Signal in the Solar Spectrum (6S) Radiative Transfer (RT) [37]; and (iv) interpolating the TOA spectrum with SkySat relative spectral response (RSR—spectral convolution). The BOA

reference spectra were employed to simulate TOA references in consideration of the image acquisition conditions (observation geometry) and the spectral properties of the sensor. The Sentinel-2 BOA time series data were from a two-year period (2019 and 2020) and the SkySat RSRs were provided freely by Planet. After the visual inspections, the RSR data of SkySat-10 were employed for all missions.

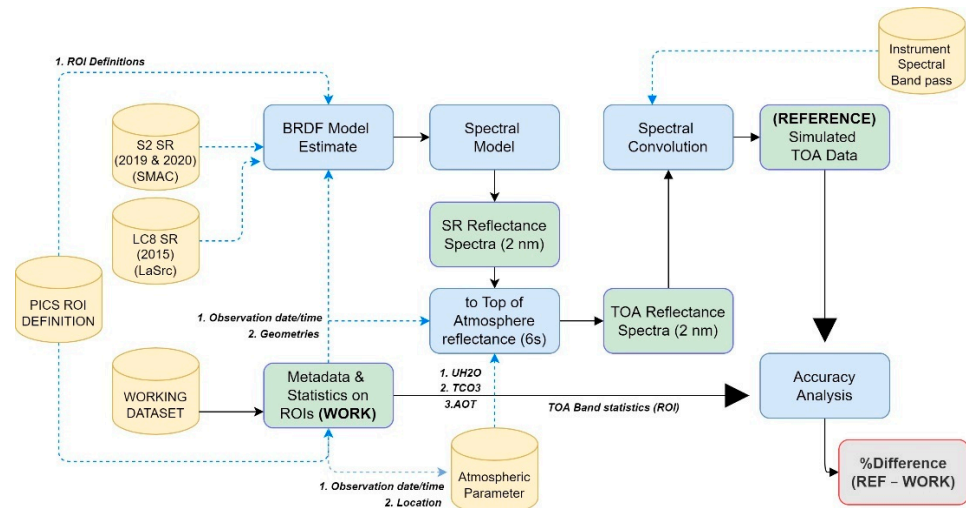


Figure 6. The workflow of absolute radiometric calibration using PICS data.

The radiometric calibration quality assessment procedure presented in Figure 6 includes:

- Surface reflectance estimation from Sentinel-2 data for the ROIs (one per SkySat camera) (Figure 7).
- Estimation of Sentinel-2 BRDF model and correction. Here, the BRDF varies linearly against scattering angle, a linear relationship between the reflectance data and scattering angle is expressed, and this is used to normalize the data.
- BOA values for each Sentinel-2 channel are estimated on the basis of the SkySat image acquisition geometries.
- BOA spectrum computation by interpolating with an interval of 2 nm.
- Atmospheric parameters are obtained at the time of image acquisition from Copernicus Atmospheric Monitoring Service (CAMS).
- Generation the TOA Spectrum using the observation geometry, atmospheric parameters and the BOA spectrum.
- Image merge per observation date, camera, and band.
- Estimation of the MS TOA values from the merged images ($TOA_{Measured}$).
- Production of simulated TOA values at SkySat band central wavelength ($TOA_{Simulated}$) by convolving the TOA Spectrum using SkySat spectral response.
- Computation of the calibration ratio (Q) and the percent difference between simulated and measured TOA values using Equation (6).

$$\%Difference = \frac{100 * (TOA_{Simulated} - TOA_{Measured})}{TOA_{Simulated}} \quad (6)$$

where:

- $TOA_{Measure}$ is the measurement processed from the SkySat product;
- $TOA_{Simulated}$ is the measurement obtained from the Sentinel-2 PICS data.

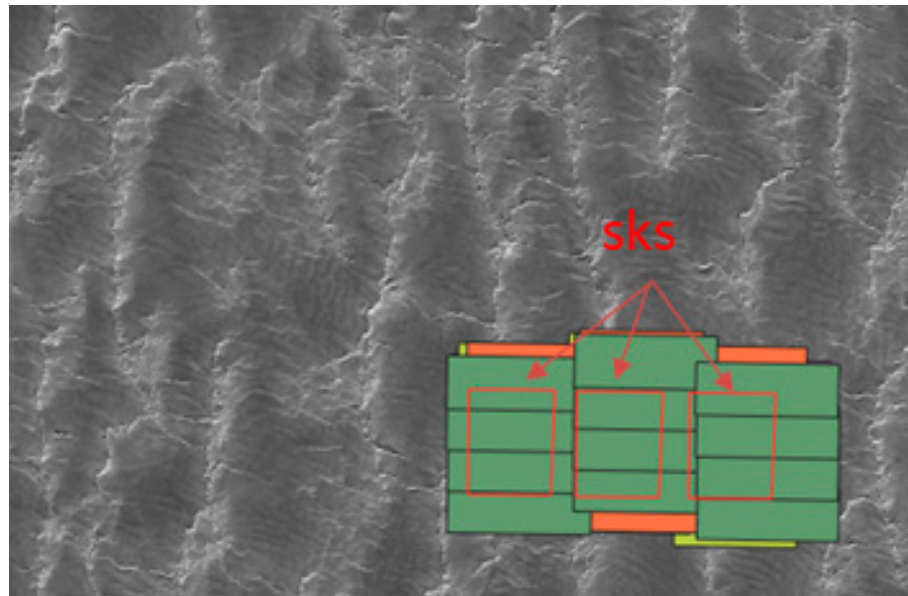


Figure 7. The SkySat scene footprint over the Libya site and the ROIs per SkySat (sks) camera.

Image data numbers (DNs) were transformed into TOA values using the coefficients given in the metadata, and the coefficients were compared with the results by using the DN-to-TOA reflectance equations. The in-band solar irradiance data were also given by the vendor (Thuillier spectrum). The Sentinel-2A (S2A) BOA values with respect to scattering angle are presented in Figure 8. The scattering angle was calculated using Equation (7). The linear correspondence between the scattering angles and the BOA measurements was used to compute the expected S2A BOA measurements for a given SkySat scattering angle. The spectral model used here is shown in Figure 9. One set of ROIs with footprints within the SkySat frame images was selected for this purpose.

$$\cos \zeta = \cos \theta \cos \vartheta + \sin \theta \sin \vartheta \cos \phi \tag{7}$$

where:

- θ, ϑ are solar/view zenith angle;
- ζ is the phase or scattering angle related to conventional angles; and
- ϕ is the “view-sun” relative azimuth angle.

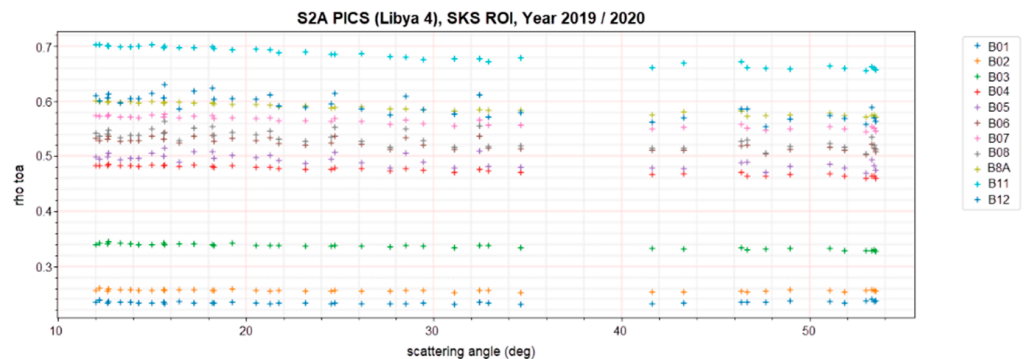


Figure 8. Input data for the BRDF modeling of Sentinel-2A time series.

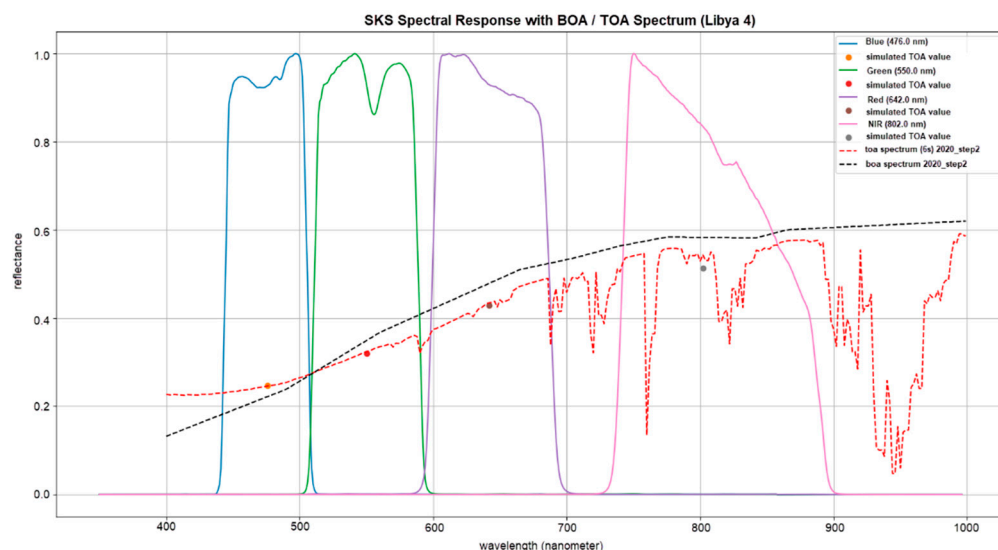


Figure 9. Simulation of TOA reflectance values for SkySat central wavelength.

2.6. Geometric Calibration Quality Assessment Approach

The geometric calibration quality was assessed using SkySat BAS and OC data from the Ankara test site (see Table 2). The BAS and OC data used for the geolocation assessments were acquired on 18 July 2020 and 23 September 2020 (Table 2) with collection GSDs of 73 cm and 66 cm, respectively. The spatial resolution of ortho products was 50 cm. The GCP distribution is given in Figure 2. The assessments were performed in terms of absolute and temporal geolocation accuracy, as well as BBR accuracy. The methods used for assessing the different accuracy assessment types were selected on the basis of the data product level (BAS or OS), the availability of georeferencing data and their format (RPC or GeoTiff), and the availability of the reference information (GCPs and dense DSMs). The methods employed here have also been used in previous scientific publications (e.g., [21,38,39]) and technical reports [22], in which further details can be found.

The absolute geolocation accuracy was assessed using a total of 44 GCPs selected on OC images and surveyed by using Global Navigation Satellite System (GNSS) instruments in the field. The assessment approaches were different for the BAS products, which were provided together with RPCs and the OC products. A ground-to-image backprojection approach was applied to the BAS products (pan only) using the GCP ground coordinates and the provided RPCs [40]. The outputs of the backprojection function were the image coordinates of the GCPs. A comparison was performed between the computed and measured image coordinates. Statistical metrics (i.e., mean, absolute mean, median, σ , and root mean square error (RMSE)) were derived from all GCPs in the x (row) and y (column) directions. The OC products were assessed by comparing the GCP ground coordinates obtained from the GNSS measurements and those obtained from the orthorectified images by manual measurements. The image measurement accuracy was assumed to be 0.5 pixels due to the manual selection of the points. The georeferencing of the OC data was defined in the Universal Transverse Mercator (UTM) Zone 36 projection system on the World Geodetic System 1984 (WGS84) datum. Similar to the BAS products, the statistical metrics were derived in the X (East–West) and Y (North–South) directions.

The temporal geolocation accuracy was obtained on the basis of a comparison of GCP coordinates measured on the OC data over Ankara. Furthermore, a dense image matching approach was applied to the two datasets. This method is based on the Kanade–Lucas–Tomasi (KLT) tracker [41], with an expected measurement accuracy of 0.1 pixel, and has been successfully applied in the assessment of lower-resolution satellite images in previous studies (e.g., [39,42,43]). The assessment was performed on the red band images, since this band has good contrast and a higher SNR.

Regarding the BBR accuracy, the KLT tracker was again employed by using the blue band as reference and the other MS bands as the search image. The discrepancies between the image coordinates in the reference and the search images of the matched keypoints were evaluated statistically to assess the BBR errors. Again, the MS BAS images acquired on 18 July 2020 and 23 September 2020 over Ankara were assessed for this purpose.

The stereoscopic capability of SkySat data was assessed by DSM generation, and the output was compared with a reference DSM obtained from the UAV data. The Catalyst software package, by PCI Geomatics, Ontario, Canada, was used for the RPC adjustment, using a total of six GCPs. Three different acquisitions over Ankara, given in Table 2, were used for this purpose. The DSM comparison was performed with the LS3D software from 4Dixplorer AG, Switzerland, and assessed in terms of the height differences between the DSMs. This approach is based on the co-registration of 3D surfaces and computation of the Euclidian distances between them as discrepancy values [44].

3. Results and Discussions

The assessment results for the SkySat maturity matrix, and the radiometric, geometric and image quality are presented and discussed in this section.

3.1. Image QA Results

The image QA assessments were performed on the basis of SNR and MTF evaluations and by means of visual inspection. With respect to the SNR measurements, more than 50 images acquired over the Libya-4 site were processed. The average SNR/SDNR (Equation (4)) results for blue, green, red and NIR bands are listed in Table 3, together with Planet's results (last column). It is worth noting that the minimal SNR requirement disclosed by Planet is 30.

Table 3. SkySat averaged SNR results for products acquired over the Libya-4 test site.

Spectral Bands	Mean SNR (ρ)	SDNR Equation (4)	σ SNR	Reference Radiance	ρ (TOA)	No. of Images	Planet's Results
Blue	134.04	57	7.78	118.33	0.23	52	34
Green	174.32	65	8.73	141.44	0.30	53	43
Red	203.98	68	7.84	158.35	0.38	53	45
NIR	190.55	58	7.40	134.48	0.46	53	41

The high reflectance of the Libya-4 site is not appropriate for assessing image SNR over the full sensor dynamic range. This limitation does not prevent performing a comparison between the EDAP and Planet results. Additionally, for all bands, the results were found to be within the SNR accuracy specification claimed by the data provider. For the same observation date, the accuracy does not vary significantly between the cameras. However, the accuracy varies depending on the satellite involved, as shown in Figure 10. The image quality of the SkySat-1 (ssc1) products is degraded compared to the image quality of the SkySat-7 (ssc7) and SkySat 10 (ssc10) products, which remain consistent.

As shown in Figure 10, a linear relationship between the SNR values and the in-band radiances exists, with a coefficient of determination (linear model estimate) reaching 0.6 for SkySat-1 products and 0.8 for SkySat-7 and SkySat-10 products, as listed in Table 4. The SNR analysis demonstrated that the image quality varies within the constellation. In this case, the accuracy loss might be due to satellite ageing, with SkySat-1 being launched in the year 2014, while SkySat-7 and SkySat-10 were launched in the year 2017.

This latter observation was also confirmed during the visual inspection. The older SkySat-1 images had a higher degree of noise than the other satellite images, and this could not be attributed to the atmosphere, which was stable during the observation period [36].

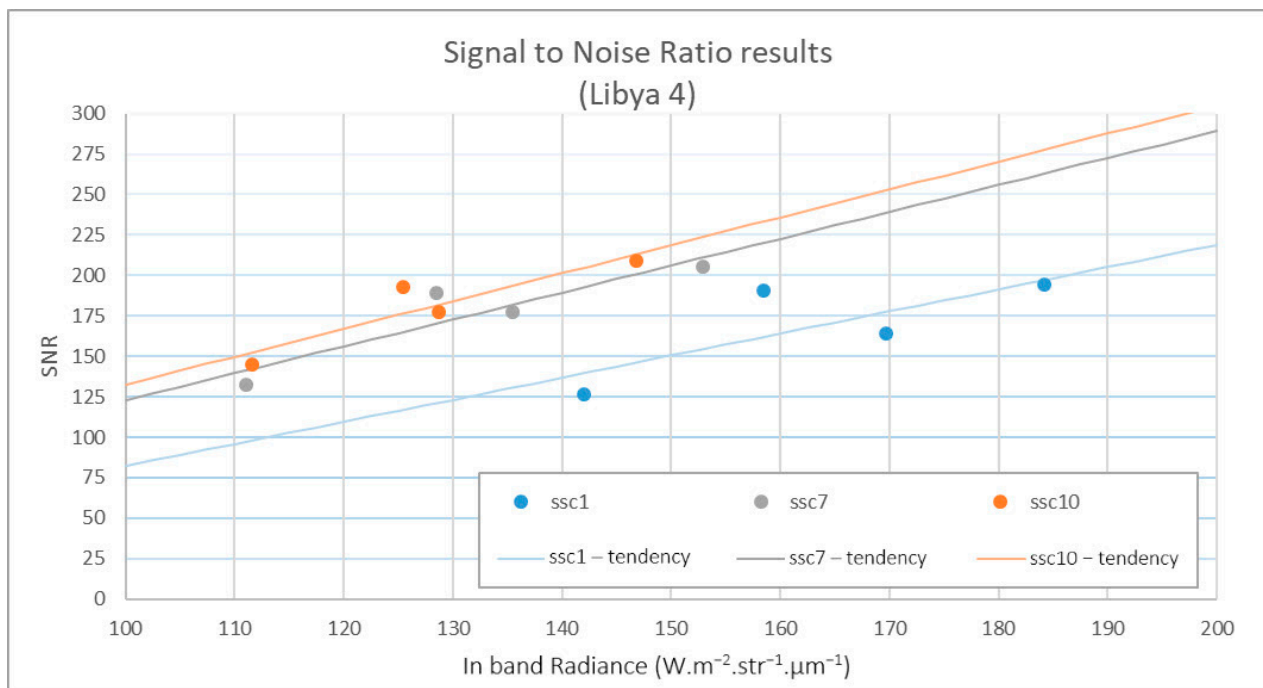


Figure 10. The mean SNR values obtained from three SkySat satellites (ssc1, ssc7, ssc10) as a function of in-band radiance and linear representation.

Table 4. The SNR and in-band radiance linear model estimate: slope (a), offset (b), and coefficients of determination.

Satellite	ssc1	ssc7	ssc10
Number of products	12	27	14
a	1.3655	1.6633	1.7235
b	−54.337	−43.45	−39.865
R ²	0.5985	0.8386	0.8288

The RER was calculated for the MS and Pan bands using edges from 5000 airports worldwide, supplied by the data provider. According to the results, the RER values were (i) blue: 0.28; (ii) green: 0.30; (iii) red: 0.34; and (iv) NIR: 0.26; Pan: 0.30. The other image quality parameters, such as FWHM and MTF value at Nyquist frequency were not shared by the provider. The results obtained here indicate that the image contrast in the MS channels at a resolution of 0.5 m was degraded, and image blurring was observed (e.g., see building rooftops in Figure 11). The pan-sharpening process applied to SkySat imagery is useful for restoring the high-frequency content, especially for urban structures (motorways, bridges, roundabouts, buildings, etc.), and performed well, resulting in the data being comparable with Pleiades images (Figure 12). Yet, as can be seen in Figures 11 and 12, the 0.5 m resolution of SkySat data is not equivalent to Pleiades in terms of image interpretability. Important drawbacks of the pan-sharpening method are that it does not preserve physical quantities in areas with low texture. Thus, these areas are smoother than the original images, resulting in a loss of image content, such as trees, crop fields, etc. In addition, on the basis of visual inspections, artefacts such as edge jitter and saturation in panchromatic images acquired over the Ankara test site were occasionally observed (Figure 13).

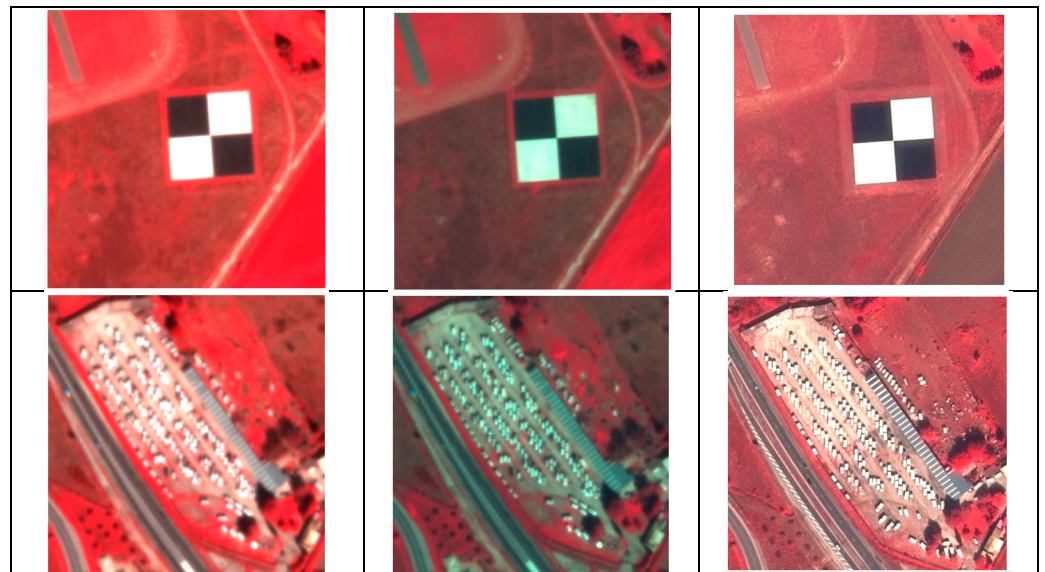


Figure 11. Examples of parts of images from the SkySat green band (**left**), the pan-sharpened green band (**middle**), and Pleiades (**right**) used for visual inspection.



Figure 12. Examples of parts of images from SkySat RGB (**left**), pan-sharpened RGB (**middle**), and Pleiades (**right**), used for visual inspection.

The MTF results obtained from the target in Salon de Provence site (Figure 14) showed that the image sharpness had decreased. The image product was at the BAS level, and was acquired on 29 December 2020. Although haze was observed in the images, this information was not available in the metadata. As can be observed from Figure 14, the dark and bright image regions were not homogeneous, and thus it cannot be considered to be a Lambertian surface, and not all artefacts can be related to the SkySat sensor. The MTF results presented in Table 5 were found to be stable in all directions. The FWHM values were larger than 2 pixels, and confirmed the blurring on the basis of reference criteria [45], which is a similar outcome to the visual inspection results. The RER values were a little worse for red and NIR channels when compared with the above-mentioned vendor results. The image quality of the different channels, in the order of best to worst, was blue, green, red, and NIR. Since the RER remained stable for all bands in different directions, the approach applied here is considered to be consistent. However, the compatibility between the RER values obtained

here and those provided by the vendor is low. In addition, the MTF results confirm a loss of contrast at the Nyquist frequency. A comparison with a true 0.5 m GSD image shows that the information content (contrast) of the SkySat image was lower, and the image sharpness decreased with 0.5 m upsampling.



Figure 13. Examples of edge jitter (**above**) and saturation (**below**) artefacts in SkySat data.

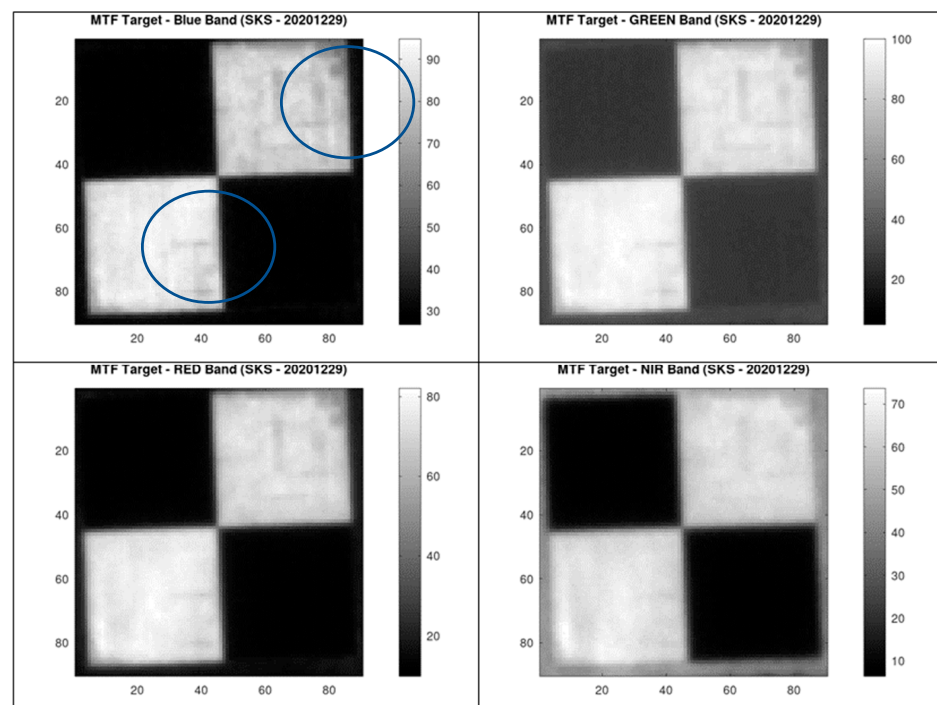


Figure 14. The SkySat image parts (29 December 2021) from the MTF target in Salon de Provence Airport and some visible degradations (blue circles). The axes are given in pixels. The legend is provided in radiance.

Table 5. The MTF results obtained from SkySat-17 BAS data acquired on 29 Dec 2020 over the Salon test site with 57 cm collection GSD and 50 cm pixel spacing. Satellite inclination angle: 53.0°.

Spectral Band and Rotation Angle	Direction of MTF Profile	MTF Along Track		MTF Across Track	
		Hh	HI	Vh	VI
Blue 2.46°	SNR	21	15	10	12
	FWHM	2.5	2.25	2	2.5
	RER	0.30	−0.31	0.29	−0.27
	MTF@Nyquist	0.05	0.04	0.06	0.05
	L_w (pixel)	14.00	19.00	16.00	16.00
	L_H (pixel)	12.75	12.75	20.25	22.75
	Delta_L *	59.74	51.49	53.01	56.61
Green 2.60°	SNR	25	15	11	12
	FWHM	2.5	2.5	2.25	2.5
	RER	0.28	−0.29	0.27	−0.26
	MTF@Nyquist	0.035	0.034	0.045	0.035
	L_w (pixel)	14.00	19.00	16.00	16.00
	L_H (pixel)	12.75	12.75	20.25	22.75
	Delta_L *	66.61	59.61	60.36	63.77
Red 2.49°	SNR	21	13	12	10
	FWHM	2.5	2.5	2	2.25
	RER	0.26	−0.26	0.26	−0.25
	MTF@Nyquist	0.04	0.025	0.035	0.031
	L_w (pixel)	14.00	19.00	16.00	17.00
	L_H (pixel)	12.75	12.75	20.25	22.75
	Delta_L *	61.44	57.32	56.71	59.54
NIR 2.68°	SNR	17	12	12	10
	FWHM	2.5	2.75	2.5	2.25
	RER	0.24	−0.23	0.24	−0.23
	MTF@Nyquist	0.03	0.03	0.02	0.04
	L_w (pixel)	12.75	12.75	20.25	22.75
	L_H (pixel)	14.00	19.00	16.00	17.00
	Delta_L *	52.62	52.83	51.05	52.37

* Delta_L = $W \cdot m^{-2} \cdot str^{-1} \cdot \mu m^{-1}$.

3.2. Radiometric Calibration QA Results

The radiometric QA results obtained here were found to be within the vendor specifications [6], and varied among the different bands (Table 6). It must be noted that the assessments performed by Planet used RadCalNet data as reference data source. By using RadCalNet measurements, a better uncertainty (2%) was expected compared to the PICS measurements (5%). Furthermore, the RadCalNet measurements were almost suitable for calibration purposes, while PICS measurements required preprocessing (simulated values). The results are the statistics of percentage difference values computed on the basis of Equation (8). The uncertainty, precision and accuracy values in Table 6 were calculated using Equations (9)–(12). It was observed that the Planet results were strongly dependent on the spectral band. The red band results were within 3%, while for the other bands, the accuracy was above 8%. However, the precision values of the Planet results remained above 20%, independently of the selected spectral bands. The mean accuracy obtained in this study was mostly below 10%, which is in accordance with the Planet results. However, it was observed that the σ value was very high. The precision values obtained (below 7%) were better than the results reported by the vendor ($\ll 28\%$). Regarding the mean accuracy, the Planet and the EDAP results were similar (below 11%), except for the red band, for which the Planet results were significantly better (2.5%). The overall uncertainty reached here was about 12%, which was also significantly better than the Planet results (25%).

Table 6. The absolute radiometric calibration uncertainty results acquired over the Libya site.

Source	Band	Accuracy	Precision	Uncertainty
EDAP	Blue	10.72%	5.69%	12.14%
	Green	8.18%	6.53%	10.46%
	Red	11.23%	4.55%	12.11%
	NIR	9.70%	4.71%	10.78%
Planet	Blue	8.58%	26.77%	28.11%
	Green	11.83%	26.42%	28.95%
	Red	2.55%	22.94%	23.08%
	NIR	8.33%	23.68%	25.10%

$$\text{Percent_difference} = 100 * (\text{Rho}_{\text{image}} - \text{Rho}_{\text{RadCalNet}}) / \text{Rho}_{\text{RadCalNet}} \quad (8)$$

$$\Delta_i = \frac{\text{Scene}_{\text{reflectance}} - \text{Site}_{\text{reflectance}}}{\text{Site}_{\text{reflectance}}} \quad (9)$$

$$\text{Accuracy} = \frac{\sum_{i=1}^n \Delta_i}{n} \quad (10)$$

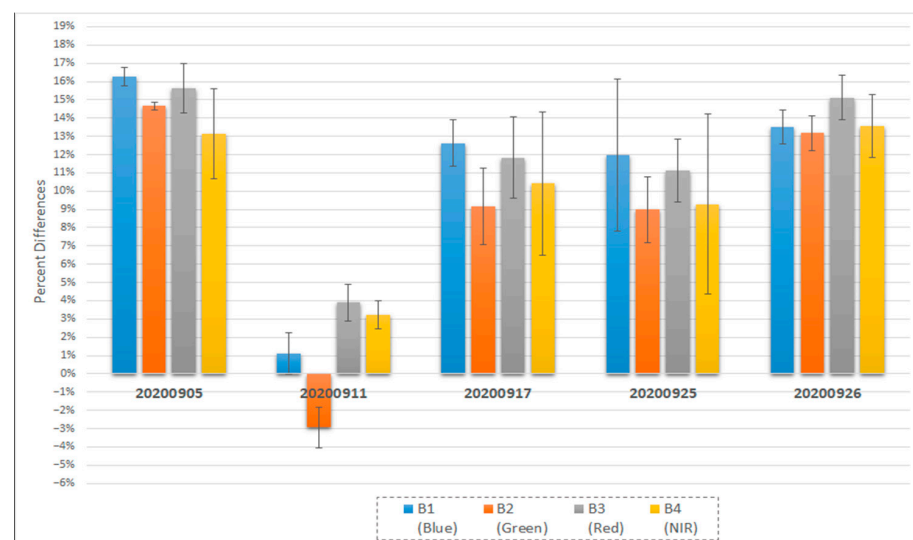
$$\text{Precision} = \sqrt{\frac{\sum_{i=1}^n (\Delta_i - \mu)^2}{n}} \quad (11)$$

$$\text{Uncertainty} = \sqrt{\mu^2 + \sigma^2} \quad (12)$$

where

- Δ_i is normalized reflectance difference;
- *Accuracy* is the mean Δ_i ;
- *Precision* is the standard deviation of Δ_i ; and
- *Uncertainty* is the root of squared sum of accuracy and precision values.

As a result of the small number of products, the test data set is not fully representative of the calibration accuracy of the constellation. Nonetheless, considering the average ROI values for a single date, it was observed that the radiometric calibration varied depending on the satellite involved, as shown in Figure 15. The strong variability between the different dates was mainly due to the satellite involved. When considering a single satellite (e.g., SkySat-7, SkySat-10), date-to-date results were in agreement with each other to within 2%, which is within the uncertainty budget of the method.

**Figure 15.** The SkySat radiometric calibration stability (September 2020) given as average results over ROIs.

The detailed results for the absolute radiometric calibration of SkySat given in Table 7 are listed with respect to observation date, depending on the ROI identifier and the detector number. As mentioned previously, the SkySat instrument embeds three independent detectors. An equivalent calibration accuracy among these three detectors is expected. The calibration accuracy of these detectors with respect to the satellite and observation dates is listed in Table 7. In most cases, even when the absolute calibration was degraded (above 10%), there were no significant differences in the results between the three different detectors. Only the SkySat-7 results exhibited large differences between detectors, and this is true for the two dates 17 September 2020 and 20 September 2020, where variability across the detectors exceed 5% in the blue and NIR bands. The calibration was stable among the detectors for SkySat-1, SkySat-10. However, it was not stable among the detectors for SkySat-7, in particular the blue band and the NIR band.

Table 7. Detailed absolute radiometric calibration results over the Libya site.

Observation Date	ROI ID	SkySat Satellite	CCD Number	Percent Difference			
				Blue	Green	Red	NIR
5 September 2020	1	10	d3	16.61%	14.51%	14.67%	11.42%
5 September 2020	2	10	d2	15.91%	14.81%	16.56%	14.88%
11 September 2020	1	1	d3	0.53%	−2.63%	3.05%	3.58%
11 September 2020	2	1	d2	0.34%	−4.18%	3.60%	2.34%
11 September 2020	3	1	d1	2.39%	−2.00%	5.03%	3.76%
17 September 2020	1	7	d1	13.01%	8.85%	10.81%	5.96%
17 September 2020	2	7	d2	13.67%	11.41%	14.41%	13.31%
17 September 2020	3	7	d3	11.19%	7.23%	10.29%	12.02%
25 September 2020	1	7	d1	16.66%	11.01%	11.34%	5.40%
25 September 2020	2	7	d2	8.74%	7.54%	9.32%	7.63%
25 September 2020	3	7	d3	10.51%	8.42%	12.70%	14.83%
26 September 2020	1	10	d3	14.24%	13.42%	14.22%	11.98%
26 September 2020	2	10	d2	12.45%	12.11%	14.64%	13.34%
26 September 2020	3	10	d1	13.86%	13.98%	16.51%	15.39%

It must be noted that the results presented here omit the daily variation, which requires further investigation in order to identify the sources of the differences (e.g., meteorological or sensor behavior). Furthermore, the calibration accuracy of the cameras may be different for different dates/times and within one image. The differences between simulated and actual TOA measurements for every product, every band and every camera show that the radiometric calibration accuracy varies among SkySat missions. The results show that the calibration of SkySat-1 (ssc1) is below 5%, irrespective of the camera. The ssc7 is temporally stable for the first (d1) and the third (d3) cameras, but unstable for the second camera (d2). Variations between the different bands were also observed for ssc7 (e.g., blue was 15% and NIR was 5.5%). The calibration results of ssc10 were temporally stable, and the results of all of the cameras were compatible (i.e., above 12% for all channels). In addition, correlations between the observation geometry properties (sun, viewing angles) and calibration results were also found.

3.3. Geometric Calibration QA Results

Here, the geometric accuracy of the absolute, relative (temporal), BBR and stereoscopic capabilities was validated. According to the vendor [6], the georeferencing accuracy specification is better than 10 m RMSE for OC products and better than 50 m for BAS products. In addition, the accuracy report provided by Planet [9] demonstrated a mean of 3.4 m mean and a σ of 2.6 m, computed from the RMSE values obtained from the absolute geolocation assessments of 50,139 ortho products. Similarly, the RMSE values obtained from the temporal geolocation assessment of 55,496 orthoimages had a mean of 3.1 m and a σ of 5.7 m. The BBR accuracy obtained on the basis of 63,900 products and expressed in mean and σ values between the different bands was also high (i.e., blue–green: 0.11 m/0.06 m;

blue–red: 0.13 m/0.08 m; blue–NIR: 0.22 m/0.14 m; green–red: 0.09 m/0.05 m; green–NIR: 0.20 m/0.12 m; red–NIR: 0.18 m/0.12 m).

The planimetric absolute geolocation accuracy values of BAS products over the Ankara test site were 1.7 m/1.3 m/1.7 m (Mean/ σ /RMSE), which were determined on the basis of two BAS products and were found to be within specifications. For the OC products, the absolute geolocation accuracy values were 1.4 m/1.1 m/1.2 m (Mean/ σ /RMSE). The temporal geolocation accuracy between the two OC products was 1.8 m/1.4 m/1.5 m (Mean/ σ /RMSE). The relative accuracy results obtained on the basis of the image matching of 1193 points exhibited comparable accuracy to the results obtained from the GCPs for the matched scenes within the uncertainty threshold of the techniques, that is, the manual measurements had lower precision compared to the image matching method used here. The BBR results defined as Mean/ σ /RMSE values were 0.03 m/0.02 m for blue–green, 0.07 m/0.05 m for blue–red, and 0.12 m/0.05 m for blue–NIR image pairs. The values were computed from six BAS products. All results were within the Planet specifications given above. A summary of all geolocation accuracy assessment results is presented in Table 8.

Table 8. SkySat geolocation uncertainty results. All results are in meters.

	BBR (mean/ σ) m	Absolute (mean/ σ) m	Temporal (mean/ σ) m
EDAP Results	Blue–green: 0.04/0.01 Blue–red: 0.07/0.02 Blue–NIR: 0.11/0.03	1.45/0.18 (BAS) 1.14/0.24 (OC)	OC: 1.51/N.A.
SkySat Q3 quality report [9]	Blue–green: 0.11/0.06 Blue–red: 0.13/0.08 Blue–NIR: 0.22/0.14	3.4/2.6	3.1/5.7

The DSM accuracy obtained from the SkySat triplet indicated a 0.55 mean shift in Z , with a σ of 2.2 m, on the basis of the comparison with the UAV DSM. The discrepancies between the SkySat and UAV DSMs are presented in Figure 16. The results obtained here indicate that the accuracy of DSM generation is affected by the temporal differences between the acquisitions, image geometry (stereo or multi-view configuration), and RPC quality. RPC improvement prior to the DSM generation is essential due to the epipolar image requirement of most dense image matching methods, e.g., semi-global matching. In this study, six GCPs were used for the selected area in order to apply a six-parameter affine correction to the RPCs of a total of eight BAS images. The global shift (0.55 m) between the SkySat and the UAV DSMs remained within the boundaries of RPC adjustment accuracy. The larger errors in the discrepancy map (Figure 16) were the result of image artefacts, cloud coverage, shadows of larger buildings, and surface changes between the acquisition dates of the SkySat dataset as well as the UAV data.

3.4. SkySat Maturity Matrix

The maturity matrix obtained from the analyses in the EDAP study is presented in Figure 17. The validation task in Figure 17 can be analyzed in terms of image quality and radiometric and geometric Cal/Val. Regarding the product information, it was observed that although the mission, products, and product format were well documented and the data were easily accessible; the algorithms used for data processing were not provided. In addition, the measurement data quality was not provided in the product format, and the traceability chain was not given. The documentation of the product generation stages included limited details. Although the documentation on the pre-flight activities was not provided, a number of documents showed that appropriate community infrastructure was used to undertake these activities. It was expected that these documents would be updated more regularly. With respect to ancillary information, we observed that useful ancillary information—including product flags with UDM set per pixel—was available. However, the product includes little information in general on ancillary data origin, ancillary data

type, uncertainties, etc. In terms of uncertainty characterization, the quality of the products is regularly monitored, and the results are reported along with a comprehensive assessment of the performances [9]. Moreover, there is a quarterly report prioritizing the documentation of image artefacts, such as parallax effects, over-sharpening, saturation, and problems in the processing chain.

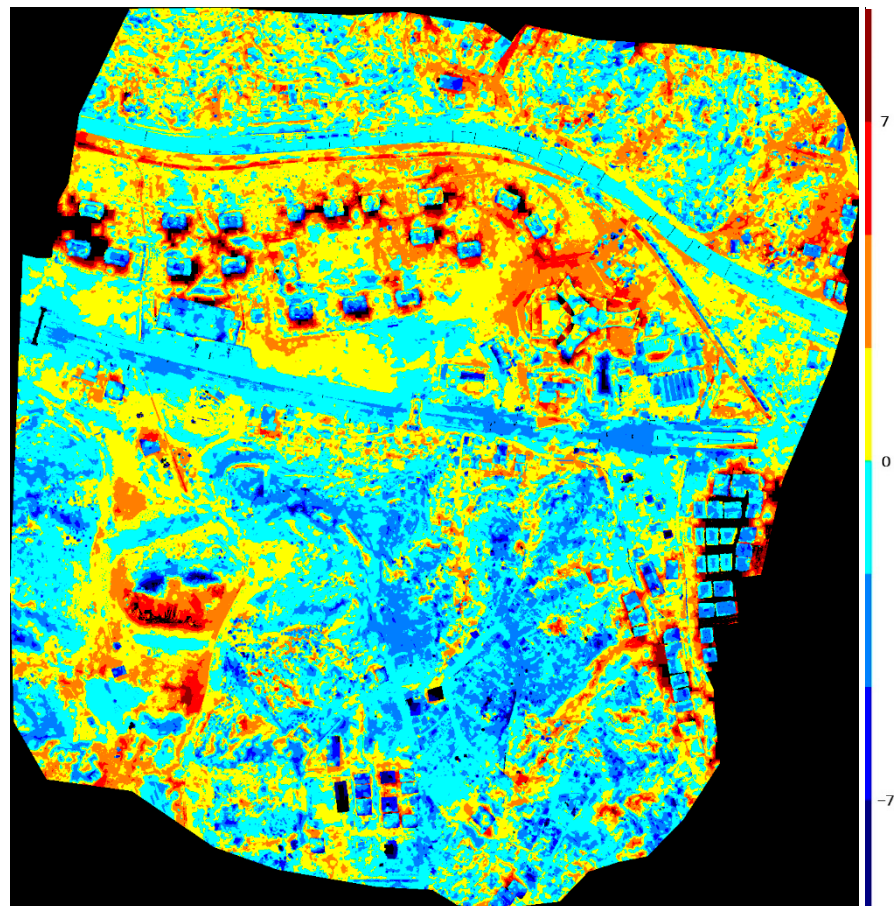


Figure 16. Discrepancy map between the SkySat and the UAV DSMs over the Ankara test site (in meters).

Product Information	Product Generation	Ancillary Information	Uncertainty Characterisation	Validation
Product Details	Sensor Calibration & Characterisation Pre-Flight	Product Flags	Uncertainty Characterisation Method 🔒	Reference Data Representativeness
Product Availability & Accessibility	Sensor Calibration & Characterisation Post-Launch 🔒	Ancillary Data	Uncertainty Sources Included 🔒	Reference Data Quality
Product Format	Retrieval Algorithm Method		Uncertainty Values Provided 🔒	Validation Method
User Documentation	Retrieval Algorithm Tuning		Geolocation Uncertainty 🔒	Validation Results
Metrological Traceability Documentation	Additional Processing			

Key
Not Assessed
Not Assessable
Basic
Intermediate
Good
Excellent
🔒 Information not public

Figure 17. SkySat maturity matrix produced in EDAP activities.

The visual inspections yielded evidence of image artefacts or anomalies that could be detected via visual checks. The SNR evaluations over the bright uniform site indicated that this parameter was stable and compliant with the Planet specification. With the MTF evaluations, the spatial resolution of the 0.5 m data was confirmed, as the processing did not alter the physical measurements of the image, and did not introduce edge overshooting, as classically observed with pan-sharpening/MTF compensation. The geometric Cal/Val assessments under the categories of absolute, temporal, BBR and stereoscopic capability showed that the results were in line with the Planet specifications [6]. The radiometric Cal/Val results obtained from the absolute calibration methodology applied to the Libya data showed that the results were heterogeneous, but remained within the specifications [6].

4. Conclusions

The analyses carried out as part of the EDAP and the results presented here show that the maturity matrix concept is valuable for the development of quality assessment standards for satellite missions and the presentation of the outcomes to users. The SkySat maturity matrix shows that the products have strengths in terms of providing product information and the characterization of uncertainty. The validation results within the EDAP also show that the products are in line with the mission specifications.

The image quality assessments were performed through radiometric calibration assessments, selected GIQE parameters, and visual inspections. The radiometric calibration assessments showed that the accuracy of the SkySat products was compliant with the specifications, and the results were within the range (< 10%) given by Planet. However, the calibration accuracy was inconsistent within the constellation, and further assessments are required using more data and possibly different external references (e.g., RadCalNet data).

The visual checks showed that the feature interpretability in the original and the pan-sharpened SkySat imagery was slightly deteriorated (blurring and smoothing were observed) in comparison to Pleiades data with similar spatial resolution. The SNR results were confirmed here for all bands and the SkySat sensors, indicating that the radiometric equalization between the cameras had been correctly performed for all configurations. On the other hand, the variation between the different sensors of the constellation can be interpreted as the aging of the platform, and must be monitored. Regarding the active PBHDR mode, the spatial resolution and the SNR and the gSNR results were upgraded using this method. It must be noted that improving SNR is an essential task for upscaling the GSD to 0.5 m. The MTF results were in accordance with the visual checks of the original MS images (without pan-sharpening), and the upsampling procedure degrades the image sharpness.

The geometric validation activities performed here involved the BBR, temporal, and absolute georeferencing accuracy, as well as stereoscopic capability (i.e., DSM generation). The BBR accuracy specification given by Planet was described in terms of band pairs. When considering the assessed bands, they were found to be within specifications [6]. The georeferencing accuracy of the BAS and OC products from two different dates was considered as well as the temporal accuracy between them, and they were also compliant with the specifications (1A: <50 m, 1C: <10 m). On the other hand, the stereoscopic capability is usually not a specification provided by vendors, and, similar to many other potential validation subjects (e.g., suitability for various application fields, minimum detectable object size, etc.), only custom assessments can be made. As future work, further validation metrics could be developed and integrated to the current scheme.

The DSM generation exercise performed here showed that the product accuracy is related to the temporal differences between the SkySat images, the image off-nadir configuration, and the RPC quality (or possibility of RPC corrections). The DSM produced from eight SkySat BAS images acquired at three different dates and off-nadir angles was compared with a UAV DSM. The global mean shift between the two DSMs was 0.55 m, with a σ of 2.4 m. The accuracy results obtained by Aati and Avouac [13] using SkySat triplets were 4 m (σ) and 5.3 m (normalized median absolute deviation), when compared with light

detection and ranging (LiDAR) data. The larger errors could be explained by the long time interval between the acquisitions of the SkySat data and the reference DSM. d'Angelo et al. (2014) obtained 1–2 m relative and 2–3 m height accuracy from a triplet using data from SkySat 1&2. The results obtained here were also in line with Bhushan et al. [14]. The DSM generation can be improved by eliminating the invalid pixels given in UDM based on the assumption that it is correct.

The main challenge in DSM validation is the correction of RPCs using GCPs, since DSMs cannot be produced without applying this procedure. A total of six GCPs were used for the dataset composed of eight BAS data with a commercial software package (PCI Catalyst). As the footprint of each BAS image is much smaller than that of push broom sensors, and one set of RPCs is provided with each, a large number GCPs is required to cover the same area as that which can be covered using Pleiades triplets. Thus, new methods and tools may be required to reduce the GCP requirement for the same area size. The SkySat image quality and the artefacts that are also affected the DSM quality, such as saturation and repetitive patterns caused by compression or noise, lead to false or no matches. Thus, larger errors were observed in such regions. As future work, radiometric preprocessing methods and image filters can be applied to improve the quality of DSM generation.

It is also considered that employing different satellite data for the EDAP would guide the development of maturity matrix standards, leading to new conclusions and future work.

Author Contributions: Conceptualization, S.S., C.A., P.G. and S.K.; methodology, S.S. and S.K.; software, S.S., I.Y. and G.K.; validation, S.S. and S.K.; formal analysis, S.S., F.D. and S.K.; investigation, S.S., F.D., I.Y., G.K. and S.K.; resources, C.A. and P.G.; data curation, S.S., C.A., F.D., R.M. and S.K.; writing—original draft preparation, S.K.; writing—review and editing, S.S., C.A., S.K. and P.G.; supervision, S.S., C.A., P.G. and S.K.; project administration, R.M. and C.A. All authors have read and agreed to the published version of the manuscript.

Funding: These activities have been funded within the framework of the ESA Earthnet Data Assessment Pilot (EDAP) project (Optical Cluster) (<https://earth.esa.int/eogateway/activities/edap> accessed on 1 February 2022). SkySat Dataset provision through the ESA EOPI Project—63602, “Quality assessment of SkySat Planet data for the Earthnet Data Assessment Pilot (EDAP)”.

Data Availability Statement: Restrictions apply to the availability of these data.

Acknowledgments: The authors are grateful to Planet for their support and the European Space Agency for provision of the SkySat data. The authors also thank to 4DiXplorer, Switzerland and Atay Muhendislik, Turkey for their support. We also would like to thank the anonymous reviewers for their valuable time and contributions.

Conflicts of Interest: The authors declare no conflict of interest.

References

1. Mannan, R.; Halsall, K.; Albinet, C.; Ottavianelli, G.; Goryl, P.; Boccia, V.; Melchiorre, A.; Piro, A.; Giudici, D.; Fox, N.; et al. ESA's Earthnet data assessment pilot: Paving the way for new space players. In Proceedings of the International Society for Optics and Photonics, Sensors, Systems, and Next-Generation Satellites XXIII, Strasbourg, France, 10 October 2019; p. 11151. [CrossRef]
2. ESA EDAP, Earthnet Data Assessment Pilot Project. 2022. Available online: <https://earth.esa.int/eogateway/activities/edap> (accessed on 3 February 2022).
3. Saunier, S.; Melchiorre, A.; Halsall, K.; Mannan, R.; Albinet, C.; Ottavianelli, G.; Goryl, P.; Boccia, V. EDAP Framework for the geometric validation of high resolution optical data. In Proceedings of the VH-RODA Workshop, Frascati, Italy, 18–22 November 2019. [CrossRef]
4. Hunt, S.E.; Albinet, C.; Nickeson, J.; Hall, A.; Fox, N.; Boccia, V.; Goryl, P. A Quality Assurance Framework for Satellite Earth Observation Missions. In Proceedings of the IEEE International Geoscience and Remote Sensing Symposium, Brussels, Belgium, 11–16 July 2021; pp. 608–611. [CrossRef]
5. Murthy, K.; Shearn, M.; Smiley, B.D.; Chau, A.H.; Levine, J.; Robinson, M.D. Sensors, Systems, and Next-Generation Satellites XVIII. In *SKS-1: Very High-Resolution Imagery from a Small Satellite*; Meynard, R., Neeck, S.P., Shimoda, H., Eds.; International Society for Optics and Photonics: Bellingham, WA, USA, 2014; Volume 9241, p. 92411E. [CrossRef]
6. Planet Imagery Product Specifications, Planet. 2020. Available online: https://assets.planet.com/docs/Planet_Combined_Imagery_Product_Specs_letter_screen.pdf (accessed on 3 February 2022).

7. EDAP.REP.001 Generic EDAP Best Practice Guidelines, 1.1, 23 May 2019. Technical Report. Available online: <https://earth.esa.int/eogateway/activities/edap/edap-best-practice-guidelines> (accessed on 1 February 2022).
8. EDAP.REP.002 Optical Mission Quality Assessment Guidelines, 1.0, 16 October 2019. Technical Report. Available online: https://earth.esa.int/eogateway/documents/20142/37627/EDAP.REP.002_1.0-Optical-Mission-Quality-Assessment-Guidelines.pdf (accessed on 1 February 2022).
9. *Planet L1 Data Quality Report Q3 2020, Status of calibration and Data Quality for the SkySat Constellation*; Technical Report Planet Labs: San Francisco, CA, USA, 2020.
10. Brunn, A.; Gonzalez, A.; Lenhard, K.; Bahloul, S.; Grennberg, J.; Smith, N.; Kinney-Spano, E.; Zuleta, I. SkySat Initial Radiometric Correction and Radiometric Calibration. In Proceedings of the JACIE Workshop, College Park, MD, USA, 17–19 September 2018. Available online: <https://calval.cr.usgs.gov/apps/sites/default/files/jacie/abrunnJACIESkySatAbsCalfin.pdf> (accessed on 3 February 2022).
11. Gonzalez, A. Absolute Calibration and Validation of SkySat Constellation. In Proceedings of the VH-RODA Workshop, Frascati, Italy, 18–22 November 2019.
12. Smiley, B. Long Term Geometric Stability of the SkySat Constellation. In Proceedings of the JACIE Workshop, College Park, MD, USA, 17–19 September 2018. Available online: <https://calval.cr.usgs.gov/apps/sites/default/files/jacie/bsmileyJACIE2018approveddraft.pdf> (accessed on 3 February 2022).
13. Aati, S.; Avouac, J.P. Optimization of Optical Image Geometric Modeling, Application to Topography Extraction and Topographic Change Measurements Using PlanetScope and SkySat Imagery. *Remote Sens.* **2020**, *12*, 3418. [[CrossRef](#)]
14. Bhushan, S.; Shean, D.; Alexandrov, O.; Henderson, S. Automated digital elevation model (DEM) generation from very-high-resolution Planet SkySat triplet stereo and video imagery. *ISPRS J. Photogramm. Remote Sens.* **2021**, *173*, 151–165. [[CrossRef](#)]
15. D’Angelo, P.; Kuschik, G.; Reinartz, P. Evaluation of skybox video and still image products. *Int. Arch. Photogramm. Remote Sens. Spat. Inf. Sci.* **2014**, *XL-1*, 95–99. [[CrossRef](#)]
16. D’Angelo, P.; Mátyus, G.; Reinartz, P. Skybox image and video product evaluation. *Int. J. Image Data Fusion* **2016**, *7*, 3–18. [[CrossRef](#)]
17. Anger, J.; Ehret, T.; Facciolo, G. Parallax estimation for push-frame satellite imagery: Application to super-resolution and 3D surface modeling from SkySat products. In Proceedings of the IEEE International Geoscience and Remote Sensing Symposium, Brussels, Belgium, 11–16 July 2021; pp. 2679–2682.
18. Valenzuela, A.Q.; Reyes, J.C.G. Comparative Study of the different versions of the General Image Quality Equation. In Proceedings of the ISPRS Annals of the Photogrammetry, Remote Sensing and Spatial Information Sciences, Enschede, The Netherlands, 10–14 June 2019; pp. 493–500. [[CrossRef](#)]
19. The National Image Interpretability Rating Scales. Available online: <https://irp.fas.org/imint/niirs.htm> (accessed on 5 March 2022).
20. Leachtenauer, J.C.; Malila, W.; Irvine, J.; Colburn, L.; Salvaggio, N. General image-quality equation: GIQE. *Appl. Opt.* **1997**, *36*, 8322–8328. [[CrossRef](#)] [[PubMed](#)]
21. Baltsavias, E.; Kocaman, S.; Wolff, K. Analysis of Cartosat-1 images regarding image quality, 3D point measurement and DSM generation. *Photogramm. Rec.* **2008**, *23*, 305–322. [[CrossRef](#)]
22. Gruen, A.; Kocaman, S. *Optical Sensors High Resolution: Geometry Validation Methodology*; Technical Report Submitted to ESA/ESRIN, RFQ/3-11780/06/I-OL; ETH Zurich, Institute of Geodesy and Photogrammetry: Zurich, Switzerland, 2008; 224p.
23. Cosnefroy, H.; Leroy, M.; Briottet, X. Selection and characterization of Saharan and Arabian desert sites for the calibration of optical satellite sensors. *Remote Sens. Environ.* **1996**, *58*, 101–114. [[CrossRef](#)]
24. Saunier, S.; Goryl, P.; Chander, G.; Santer, R.; Bouvet, M.; Collet, B.; Mambimba, A.; Aksakal, S.K. Radiometric, geometric, and image quality assessment of ALOS AVNIR-2 and PRISM sensors. *IEEE Trans. Geosci. Remote Sens.* **2010**, *48*, 3855–3866. [[CrossRef](#)]
25. Bouvet, M. Intercomparison of multispectral imagers over natural targets. In Proceedings of the IEEE International Geoscience and Remote Sensing Symposium, Barcelona, Spain, 23–28 July 2007; pp. 2653–2664. [[CrossRef](#)]
26. Murakami, H.; Tadono, T.; Imai, H.; Nieke, J.; Shimada, M. Improvement of AVNIR-2 Radiometric Calibration by Comparison of Cross-Calibration and Onboard Lamp Calibration. *IEEE Trans. Geosci. Remote Sens.* **2009**, *47*, 4051–4059. [[CrossRef](#)]
27. Chander, G.; Meyer, D.J.; Helder, D.L. Cross calibration of the Landsat-7 ETM+ and EO-1 ALI sensor. *IEEE Trans. Geosci. Remote Sens.* **2004**, *42*, 2821–2831. [[CrossRef](#)]
28. Robinson, D. High-resolution imagery and video from SkySat-1. In Proceedings of the Joint Agency Commercial Imagery Evaluation (JACIE), Louisville, KY, USA, 26–28 March 2014.
29. SkySat Instruments. Available online: <https://earth.esa.int/eogateway/missions/skysat> (accessed on 6 March 2022).
30. Thome, K.J. Post-Launch Calibration of Satellite Sensors. In *In-Flight Intersensor Radiometric Calibration Using Vicarious Approaches*, 1st ed.; Morain, S.A., Budge, A.M., Eds.; Balkema Publishers: London, UK, 2004; pp. 93–102. ISBN 90 5809 693 9.
31. Zaroni, V.; Ryan, R.; Holekamp, K.; Pagnutti, M. IKONOS Signal-to-Noise Ratio Estimation. In Proceedings of the JACIE Workshop, Reston, VA, USA, 25–27 March 2002. Available online: <https://ntrs.nasa.gov/api/citations/20040004380/downloads/20040004380.pdf> (accessed on 21 November 2021).
32. Viallefont-Robinet, F.; Helder, D.; Fraisse, R.; Newbury, A.; van den Bergh, F.; Lee, D.; Saunier, S. Comparison of MTF measurements using edge method: Towards reference data set. *Opt. Express* **2018**, *26*, 33625–33648. [[CrossRef](#)] [[PubMed](#)]

33. Blanc, P.H. Calibration Test Sites Selection and Characterisation–WP210. *Technical Report TN-WP210-001-ARMINES submitted to ESA/ESRIN*; VEGA Technologies SAS, 4 March 2008. Available online: http://calvalportal.ceos.org/c/document_library/get_file?uuid=03407bb4-89e4-4271-be26-898298780ee7&groupId=10136 (accessed on 1 February 2022).
34. Kohm, K. Modulation transfer function measurement method and results for the Orbview-3 high resolution imaging satellite. In *Proceedings of the International Archives of the Photogrammetry, Remote Sensing and Spatial Information Sciences (ISPRS Arch)*, Istanbul, Turkey, 12–23 July 2004; Volume 35, pp. 7–12.
35. Yalcin, I.; Kocaman, S.; Saunier, S.; Albinet, C. Radiometric Quality Assessment for Maxar HD Imagery. In *Proceedings of the International Archives of Photogrammetry, Remote Sensing and Spatial Information Sciences*, Niece, France, 5–9 July 2021; pp. 797–804. [[CrossRef](#)]
36. Saunier, S.; Kocaman, S. EDAP Technical Note on Quality Assessment for SkySat. Issue 1.0. 6 September 2021. Available online: https://earth.esa.int/eogateway/documents/20142/37627/EDAP.REP.015+TN+on+Quality+Assessment+for+SkySat_v1.0.pdf/59a2a91d-eecd-20f1-4a13-e670dad8eed3 (accessed on 28 January 2022).
37. Artmo. 2021. Available online: <https://artmotoolbox.com/radiative-transfer-models/89-atmospheric-rtms/27-6sv.html> (accessed on 3 February 2021).
38. Aksakal, S.K.; Neuhaus, C.; Baltasvias, E.; Schindler, K. Geometric quality analysis of AVHRR orthoimages. *Remote Sens.* **2015**, *7*, 3293–3319. [[CrossRef](#)]
39. Kocaman, S.; Debaecker, V.; Bas, S.; Saunier, S.; Garcia, K.; Just, D. A Comprehensive Geometric Quality Assessment Approach for MSG SEVIRI Imagery. *Adv. Space Res.* **2021**, *69*, 1462–1480. [[CrossRef](#)]
40. Fraser, C.S.; Dial, G.; Grodecki, J. Sensor orientation via RPCs. *ISPRS J. Photogramm. Remote Sens.* **2006**, *60*, 182–194. [[CrossRef](#)]
41. Lucas, B.D.; Kanade, T. An iterative image registration technique with an application to stereo vision. In *Proceedings of the 7th International Joint Conference on Artificial Intelligence*, Vancouver, BC, Canada, 24–28 August 1981; pp. 674–679.
42. Bas, S.; Debaecker, V.; Kocaman, S.; Saunier, S.; Garcia, K.; Just, D. Investigations on the Geometric Quality of AVHRR Level 1B Imagery Aboard MetOp-A. *PFG–J. Photogramm. Remote Sens. Geoinf. Sci.* **2021**, *89*, 519–534. [[CrossRef](#)]
43. Debaecker, V.; Kocaman, S.; Saunier, S.; Garcia, K.; Bas, S.; Just, D. On the Geometric Accuracy and Stability of MSG SEVIRI Images. *Atmos. Environ.* **2021**, *262*, 118645. [[CrossRef](#)]
44. Gruen, A.; Akca, D. Least squares 3D surface and curve matching. *ISPRS J. Photogramm. Remote Sens.* **2005**, *59*, 151–174. [[CrossRef](#)]
45. USGS Spatial Resolution Digital Imagery Guideline. Available online: <https://www.usgs.gov/media/images/spatial-resolution-digital-imagery-guideline> (accessed on 1 February 2022).